

# Oxygen-Induced Reversible Sn-Dopant Deactivation between Indium Tin Oxide and Single-Crystalline Oxide Nanowire Leading to Interfacial Switching

Hao Zeng, Tsunaki Takahashi,\* Takehito Seki, Masaki Kanai, Guozhu Zhang, Takuro Hosomi, Kazuki Nagashima, Naoya Shibata, and Takeshi Yanagida\*



Cite This: *ACS Appl. Mater. Interfaces* 2020, 12, 52929–52936



Read Online

ACCESS |



Metrics & More



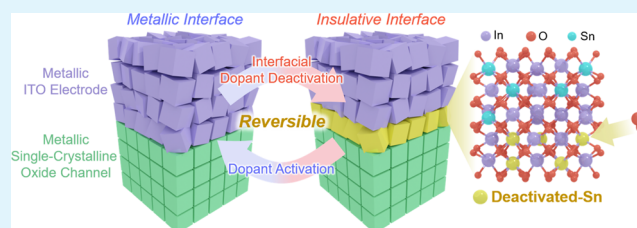
Article Recommendations



Supporting Information

**ABSTRACT:** An impurity doping in semiconductors is an important irreversible process of manipulating the electrical properties of advanced electron devices. Here, we report an unusual reversible dopant activation/deactivation phenomenon, which emerges at an interface between indium tin oxide (ITO) and single-crystalline oxide channel. We found that the interface electrical resistance between ITO electrodes and single-crystalline oxide nanowire channel can be repeatedly switched between a metallic state and a near-insulative state by applying thermal treatments in air or vacuum. Interestingly, this electrical switching phenomenon disappears when the oxide nanowire changes from the single-crystalline structure to the lithography-defined polycrystalline structure. Atmosphere-controlled annealing experiments reveal that atmospheric oxygen induces repeatable change in the interfacial electrical resistance. Systematic investigations on metal cation species and channel crystallinity demonstrate that the observed electrical switching is related to an interface-specific reversible Sn-dopant activation/deactivation of ITO electrode in contact with a single-crystalline oxide channel.

**KEYWORDS:** interface resistance, metal oxide nanowires, indium tin oxide (ITO), electrical switching, dopant activation/deactivation



## INTRODUCTION

Heterointerfaces of metal oxides exhibit interesting physical and chemical properties, including resistive switching, superconductivity, magnetism, ion transport, catalytic ability, and others.<sup>1–6</sup> Various nanostructures, including heteroepitaxial thin films, core–shell nanostructures, and/or nanoparticle-decorated nanostructures, have been fabricated and employed to study such interfacial properties.<sup>7–10</sup> Among these nanostructures of metal oxides, single-crystalline metal oxide nanowire is an ideal platform to extract intrinsic interfacial properties due to the well-defined crystal facets, grain-boundary-free carrier transport, and high surface-to-volume ratio.<sup>11–15</sup> For the electrical measurements of such metal oxide nanowire, various metallic electrode materials (typically Pt, Au, Ti, Cr, or degenerately doped semiconductors) have been examined to achieve mostly Ohmic contact (or Schottky contact).<sup>12</sup> Among such electrodes, indium tin oxide (ITO), which is one of the most popular transparent electrodes for mass-produced electronic devices,<sup>16–18</sup> is a promising electrode on metal oxide nanowire channels because of its high and stable electrical conductivity even at high humidities and/or high temperatures. For example, fully transparent transistors for photodetectors and flexible electronics, core–shell nanowire array photovoltaic devices, and humidity sensors have been achieved using oxide nanowire channels

with ITO transparent electrodes.<sup>10,19–22</sup> Thus, major interest of ITO electrodes on nanoscale metal oxide channels has been directed to utilize the metallicity and transparency of ITO electrodes.<sup>23,24</sup> To the best of our knowledge, none of the previous works has dealt with the interfacial electrical properties of metallic ITO electrodes in contact with nanoscale metal oxide channels, because it has been believed that ITO metallic nanocontact is robust under harsh environments such as high temperatures.

In this study, we report an unusual reversible dopant activation/deactivation phenomenon, which only emerges at an interface between ITO electrodes and single-crystalline oxide channel. The interface resistance between the ITO electrodes and degenerately doped single-crystalline oxide nanowire channels was repeatedly switched with a resistance ratio of nearly 4 orders of magnitude via thermal treatment in air or vacuum. Atmosphere-controlled annealing experiments reveal that only atmospheric oxygen is responsible for the

**Received:** September 7, 2020

**Accepted:** October 28, 2020

**Published:** November 10, 2020



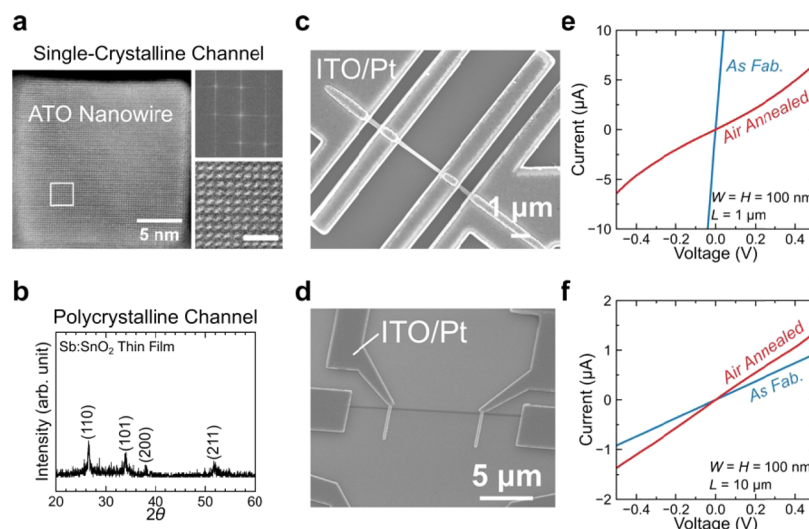


**Figure 1.** (a) Cross-sectional HAADF STEM images of a typical VLS-grown ATO nanowire (as-fabricated). Fast Fourier transform pattern of the whole nanowire region and the close-up image of the boxed area (bar: 1 nm) are also shown. (b) XRD pattern of polycrystalline ATO (Sb/SnO<sub>2</sub>) thin film after air annealing (400 °C, 10 min). FESEM images of (c) single-crystalline and (d) polycrystalline ATO channel devices. *I*–*V* characteristics of (e) single-crystalline and (f) polycrystalline ATO channel devices with ITO electrodes, including both as-fabricated and air-annealed (400 °C, 10 min) devices. *W*, *H*, and *L* are channel width, height, and length, respectively.

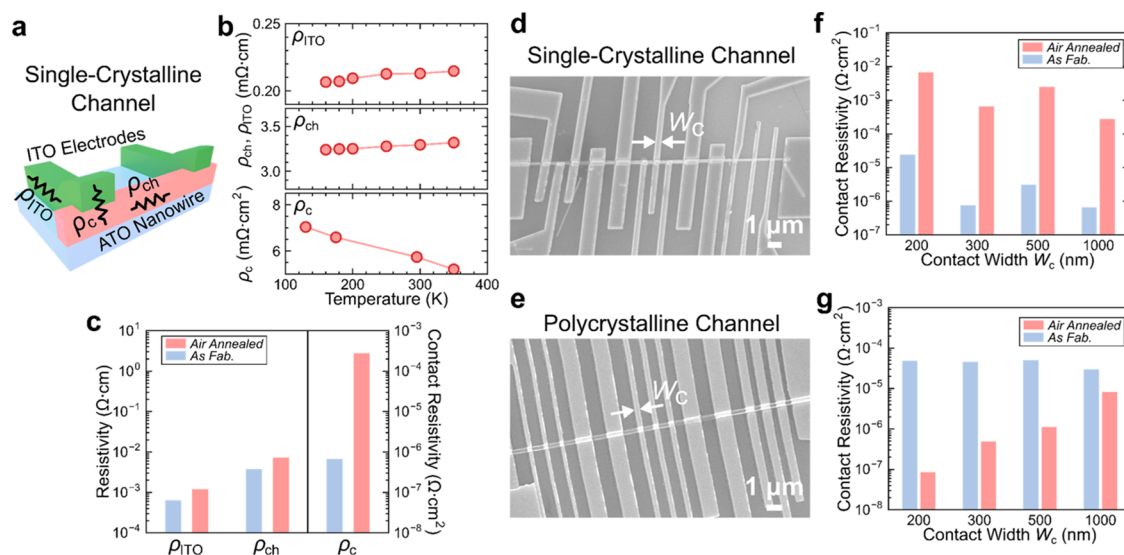


**Figure 2.** (a) Cross-sectional schematic image of single-crystalline oxide channel device. (b) Temperature dependence of resistivities of ITO electrode ( $\rho_{\text{ITO}}$ ), single-crystalline ATO channel ( $\rho_{\text{ch}}$ ), and contact resistivity ( $\rho_{\text{c}}$ ) after air annealing (400 °C, 10 min). (c)  $\rho_{\text{ITO}}$ ,  $\rho_{\text{ch}}$ , and  $\rho_{\text{c}}$  just after fabrication (As Fab) and after air annealing (400 °C, 10 min). FESEM images of multielectrode (d) single-crystalline ATO channel and (e) polycrystalline ATO channel devices. Contact resistivity for various contact electrode width ( $W_{\text{c}}$ ) within multielectrode (f) single-crystalline and (g) polycrystalline ATO channel devices, including both as-fabricated and air-annealed (400 °C, 10 min) devices.

repeatable change in the interfacial resistance. We found that the observed electrical switching is related to an interface-specific reversible Sn-dopant activation/deactivation of the ITO electrode in contact with single-crystalline oxide channel.

## RESULTS AND DISCUSSION

First, we examine the electrical characteristics between ITO electrodes and the two types of degenerately n-type Sb-doped SnO<sub>2</sub> (ATO: antimony-doped tin oxide) nanowire channels: single-crystalline channel and polycrystalline channel. Figure 1a shows the cross-sectional high-angle annular dark-field (HAADF) scanning transmission electron microscopy (STEM) images of ATO nanowires grown via the vapor-liquid-solid (VLS) process using pulsed-laser deposition

(PLD).<sup>25,26</sup> The image shows the crystal-faceted square shape, highlighting the single-crystalline structure. Polycrystalline ATO channel devices were fabricated by patterning of a deposited ATO thin film. Figure 1b shows the X-ray diffraction (XRD) pattern of ATO films grown on growth conditions identical to those of polycrystalline ATO channel devices. The observed XRD peaks corresponding to the SnO<sub>2</sub> rutile structure indicate the polycrystalline structure of ATO films onto amorphous SiO<sub>2</sub>.<sup>27,28</sup> Figure 1e,f shows the comparison between single-crystalline and polycrystalline ATO channels on the *I*–*V* characteristics using ITO electrodes when thermal air annealing (400 °C, 10 min) was performed. Clearly, the two devices showed completely different trends on the effect of air annealing on *I*–*V* characteristics. Before air annealing, good

Ohmic and low-resistance electrical characteristics were consistently observed in both two devices. However, the effect of thermal air annealing is rather different on the two devices. Non-Ohmic  $I$ - $V$  and a significant increase of electrical resistance were observed only for the single-crystalline channel device (Figure 1e, from 4.0 to 100 k $\Omega$ ). On the contrary, the resistance of the polycrystalline channel device slightly decreased due to air annealing (Figure 1f, from 540 to 350 k $\Omega$ ), which is a general trend of thermal annealing via improvement of crystallinity, removal of residual impurities, and others.<sup>11,29,30</sup> The improvement of crystallinity of ATO polycrystalline channel material via annealing was observed in the XRD patterns of the ATO film at varied annealing temperatures, supporting this model (Figure S1). This observed significant difference between the two devices on the effect of air annealing is rather unique because the structural difference between the two devices is solely the crystallinity of oxide channel in contact with identical ITO electrodes.

Here, we question where the observed resistance increase of single-crystalline ATO channel device occurs, at (1) ITO electrodes, (2) ATO channel, or (3) the interface, during annealing (Figure 2a). Four-probe measurements of air-annealed ITO electrode thin-film and single-crystalline ATO channel device were performed to answer this question. For the temperature dependence of the resistivities of ITO thin film and single-crystalline ATO channel, both the ITO electrodes and the ATO channel showed metallic electrical conduction and sufficiently low resistivities ( $\sim 10^{-3}$   $\Omega$ -cm, Figure 2b,c) even after air annealing, compared with the reported values for each material.<sup>31,32</sup> Therefore, the resistance change of single-crystalline ATO channel device observed in Figure 1 cannot be interpreted in terms of resistivity changes of either ITO electrode or ATO channel. Then, the electrical resistivity at the interface between the ITO electrodes and ATO channel (contact resistivity) was extracted. A substantial increase in the contact resistivity, up to 4 orders of magnitude compared to as-fabricated devices, was observed after air annealing (Figure 2c). The interface resistance shows semi-conducting or insulating temperature dependence (Figure 2b), and this interface insulation effect occurs within 10 min of air annealing (Figure S2). Since the ITO electrodes and ATO channels themselves maintain sufficiently low resistivities during air annealing, this interface insulation is the origin of the change of  $I$ - $V$  characteristics after air annealing (Figure 1e). Note that the contact resistivity of the polycrystalline channel device decreased after air annealing (Figure S3), yielding the general improvement of  $I$ - $V$  characteristics (Figure 1f). In addition, the effects of contact width of ITO electrodes on the interfacial insulation behavior were systematically investigated using multielectrode devices, as shown in Figure 2d-g. The interfacial insulation was consistently observed only in single-crystalline channel devices independent of the contact width, indicating that electrode dimension is not the cause of this interfacial insulation. It is noted that this interfacial electrical insulation between metallic ITO and nanoscale single-crystalline oxide channels has not been reported in the previous studies that employed ITO electrodes in metal oxide semiconductor devices.<sup>8,19,21,33-35</sup>

Although the above results reveal the significant role of air annealing in the interfacial electrical resistance of single-crystalline ATO channel in contact with ITO electrodes, it is still not clear which molecular species in air cause such

interfacial electrical insulation. Since a redox event plays an important role in the carrier density of n-type oxide semiconductor-ATO via altering the oxygen contents,<sup>29,36</sup> we perform annealing steps in both oxidizing and reducing atmospheres ( $\text{NO}_2$ ,  $\text{O}_2$ , and  $\text{H}_2$ ). Figure 3a shows the contact

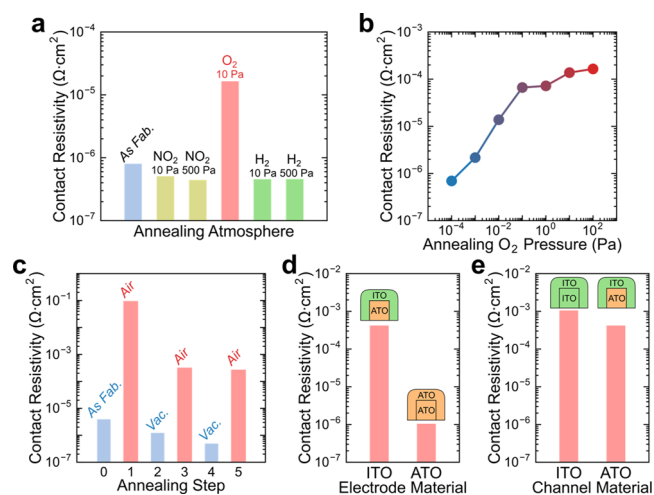


**Figure 3.** (a) Contact resistivity of ITO-contacted single-crystalline ATO channel devices under a series of annealing steps under various atmospheric conditions. The concentration of  $\text{NO}_2$ ,  $\text{O}_2$ , and  $\text{H}_2$  was 100 ppm, with Ar used as a base gas. (b) Annealing oxygen pressure dependence of the contact resistivity of ITO-contacted single-crystalline ATO channel device. (c) Contact resistivity of ITO-contacted single-crystalline ATO channel devices under sequential annealing steps alternately in air and under vacuum. All annealings were performed at 400 °C for 10 min. (d) Contact resistivities of single-crystalline ATO channel devices with ITO and ATO electrodes. (e) Contact resistivities of single-crystalline ATO and ITO channel devices with ITO electrodes. All contact resistivities were measured after air annealing at 400 °C for 10 min.

resistivities of single-crystalline ATO channel devices with ITO electrodes after annealing in  $\text{NO}_2$ ,  $\text{O}_2$ , and  $\text{H}_2$  atmospheres. Clearly, only the oxygen annealing increased the contact resistivity (i.e., interfacial insulation) while  $\text{NO}_2$  and  $\text{H}_2$  annealing did not exhibit such interfacial insulation and slightly decreased contact resistivity. Since both  $\text{NO}_2$  (oxidizing) and  $\text{H}_2$  (reducing) annealing did not significantly alter the contact resistivities, the observed interfacial insulation cannot be interpreted solely in terms of simple redox-based model.<sup>29,37</sup> To further confirm the atmospheric oxygen-induced scenario, we examine the effect of oxygen partial pressure during annealing on the contact resistivities of single-crystalline ATO channels with ITO electrodes, as shown in Figure 3b. Clearly, increasing the oxygen partial pressure monotonically increased the contact resistivity, which further confirms the significant role of atmospheric oxygen on the observed interfacial insulation. Note that the variation of channel resistivity is much smaller than that of the contact resistivity (Figure S4). The interfacial insulation begins even a tiny oxygen amount ( $\sim 10^{-3}$  Pa) is present and progresses continuously as the oxygen pressure increases. More interestingly, the oxygen-induced interfacial insulation completely recovers to near the as-fabricated value by performing vacuum annealing and increases again upon subsequent air annealing (Figure 3c). Note that these interface resistance changes are not observable at the interface between metallic ITO and polycrystalline ATO channels. Thus, these exper-

**Table 1. Resistivities and Contact Resistivities of Single-Crystalline Oxide Channel Devices<sup>a</sup>**

	electrodes/channel	as fab.	air-annealed
resistivity, $\rho_{\text{ITO}}, \rho_{\text{ATO}}, \rho_{\text{ch}}$ ( $\Omega\text{-cm}$ )	ITO electrode	$6.4 \times 10^{-4}$	$1.2 \times 10^{-3}$
	ATO channel	$8.5 \times 10^{-3}$	$1.6 \times 10^{-2}$
	ITO channel	$1.3 \times 10^{-2}$	$1.4 \times 10^{-2}$
	ATO electrode	$3.0 \times 10^5$	$1.2 \times 10^{-1}$
	ATO channel		$1.3 \times 10^{-2}$
	ITO channel		$3.2 \times 10^{-2}$
contact resistivity, $\rho_c$ ( $\Omega\text{-cm}^2$ )	ITO/ATO channel	$9.1 \times 10^{-7}$	$4.2 \times 10^{-4}$
	ITO/ITO channel	$1.1 \times 10^{-6}$	$1.1 \times 10^{-3}$
	ATO/ATO channel		$1.1 \times 10^{-6}$
	ATO/ITO channel		$1.0 \times 10^{-6}$

<sup>a</sup>Resistivities of ATO electrodes ( $\rho_{\text{ATO}}$ ),  $\rho_{\text{ITO}}$ ,  $\rho_{\text{ch}}$ , and  $\rho_c$  of both single-crystalline ATO and ITO channel devices with ATO or ITO electrodes. Resistivities of as-fabricated (as fab.) and air-annealed devices are shown. The  $\rho_{\text{ATO}}$  value was notably high ( $>10^5 \Omega\text{-cm}$ ) immediately after deposition, the details of which are described in the Methods section. Therefore,  $\rho_{\text{ch}}$  and  $\rho_c$  of the as-fabricated devices with ATO electrodes were not measured.

imental results highlight that the observed interfacial electrical resistance change is unexpectedly reversible, and atmospheric oxygen induces the electrical change only at the interface between metallic ITO and nanoscale single-crystalline ATO channels.

Next, we examine what interfacial material combinations are required to exhibit the atmospheric oxygen-induced reversible interfacial resistance change. Figure 3d shows the effect of electrode materials (ITO and ATO) on the contact resistivities of single-crystalline ATO channels. The detailed data on the fabrication and characterization of ATO electrodes are provided in the previous work<sup>38</sup> and Figure S1, and the contact resistivity data were measured after air annealing. As can be seen in the figure, only the device with ITO electrode exhibited the interfacial electrical insulation but not for that with the ATO electrode, highlighting the significant role of ITO electrode in the reversible interfacial insulation. We further examine the effect of single-crystalline channel materials on the contact resistivities of those channels in contact with ITO, as shown in Figure 3e. Single-crystalline ITO nanowires were grown by the Au-catalyzed PLD method, as previously reported,<sup>39</sup> and the detailed fabrication conditions are shown in the Methods section. Interestingly, both single-crystalline channel devices exhibited the interfacial electrical change. A detailed summary of resistivities of the electrodes, channels, and their interfaces for both as-fabricated and air-annealed devices is presented in Table 1. Clearly, only the devices with ITO electrodes exhibited electrical change at the electrode/channel interfaces. From a different perspective, ATO electrodes have better thermal stability than ITO electrodes because the low contact resistivity can be maintained even after air annealing. Thus, these experimental results highlight that ITO electrodes in contact with nanoscale single-crystalline oxide channels are required to exhibit a reversible interfacial electrical change induced by atmospheric oxygen.

Since the observed reversible interfacial electrical change occurs at several orders of magnitudes, one plausible model to explain this huge electrical change is solely based on the existence of some microscopic structural changes at the interface, which are electrically insulative. Thus, we perform STEM analysis to examine whether microscopic structural changes are induced at the interface during reversible resistance change via atmospheric oxygen. Figure 4a,b shows the cross-sectional HAADF STEM images of the air-annealed

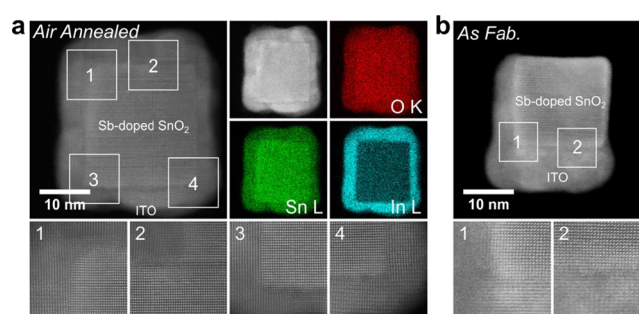


**Figure 4.** Cross-sectional HAADF STEM images of single-crystalline ATO nanowire (core)/ITO electrode (shell) structure (a) after air annealing (400 °C, 10 min) and (b) just after fabrication (as fab.). Energy-dispersive X-ray spectrometer (EDX) images of the core/shell structure (O-K, Sn-L, and In-L edges) are also shown for air-annealed sample.

and as-fabricated single-crystalline ATO nanowire (core)/ITO electrode (shell) structure, respectively. The details of TEM sample preparation are provided in the Methods section. Single-crystalline structure and oriented-grain structures with low-angle grain boundary are observed for the ATO channel core and ITO electrode shell after air annealing, respectively. The clear oriented-grain structure of the ITO electrode shell was formed during air annealing (Figure 4a,b). As can be seen in the image, there are no distinct intermediate layers or specific structures at the interface between the ATO channel and the ITO electrode. Energy-dispersive X-ray spectrometry (EDX) was also performed to analyze the element distribution at the interface. The EDX mapping images of O-K, Sn-L, and In-L edges for the air-annealed sample are shown in Figure 4a. Similar to the HAADF images, any specific features such as element segregations at the interface are not observable. The HR-STEM analyses indicate that an oxygen-induced reversible interfacial resistance change occurs at least without observable structural electrically insulative byproducts at the interface, and another model has to be considered to explain the observed reversible interfacial insulation.

Oxygen-induced Sn-dopant deactivation within ITO electrodes at an interface between ITO electrodes and single-crystalline channels is the other possible model. A formation of Sn–O<sub>i</sub> (O<sub>i</sub> denoting interstitial oxygen) clustering within ITO-bixbyite crystal structure, which occurs below the spatial resolution of the current HR-STEM techniques, could be a mechanism of Sn-dopant deactivation. The reason why such

interstitial oxygens can be assumed is that a bixbyite crystal structure of ITO has inherently two vacancy sites of a close-packed fluorite crystal structure.<sup>40,41</sup> Theoretical and experimental studies have reported that interstitial oxygen reacts with Sn-dopant ions to form neutral Sn–O<sub>i</sub> clusters ((2Sn<sup>+</sup>–O<sub>i</sub><sup>2-</sup>), resulting in an oxygen-induced dopant deactivation in ITO.<sup>40,42–48</sup> Our experimental results on the air-annealing temperature dependence of contact resistivity are qualitatively consistent with this model based on the formation of Sn–O<sub>i</sub>. As shown in Figure 5, the contact resistivity has a maximum

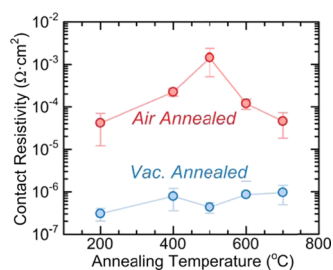


**Figure 5.** Air- or vacuum-annealing temperature dependence of contact resistivity of single-crystalline ATO channel devices with ITO electrodes. All annealings were performed for 10 min.

value in its air-annealing temperature dependence, indicating that the reversible interfacial resistance change mechanism is most effective in the temperature range around 500 °C. This trend is also consistent with oxygen-induced dopant deactivation model because the existence of an optimal temperature for the interfacial resistive change can be understood through the thermodynamic dependence of interstitial oxygen density in metal oxides annealed in oxygen-containing atmospheres.<sup>49</sup> Since a Sn–O<sub>i</sub> clustering phenomenon should not be limited to nanowire channels, we examine the existence of reversible interfacial resistance change for single-crystalline ITO film<sup>50,51</sup> devices with ITO electrodes, as shown in Figure S5. The details of the fabrication and characterization of ITO films are provided in the Supporting Information. The reversible interfacial resistance change is also observed at an interface between the ITO electrode and the single-crystalline ITO film channel. Although these experimental results consistently support the Sn-dopant deactivation induced by Sn–O<sub>i</sub> clustering to explain the observed reversible interfacial resistance change, there are several interesting issues to further understand the origin of reversible interfacial insulation. For example, there are no appropriate explanations for why such Sn–O<sub>i</sub> clustering preferentially occurs at the interface between the ITO electrode and single-crystalline ATO channels and not on the polycrystalline ATO channel. In addition, during the transition from initial metallic contacts into an insulating interface, the entire ITO contact area surrounding the channel must be completely depleted via Sn–O<sub>i</sub> clustering. The potential barrier at this interface induced by oxygen adsorption is an additional possible model to explain why the interfacial switching occurs only in single-crystalline channel devices. Previous studies of electronic structures at grain boundaries of polycrystalline oxide semiconductors have reported that excess oxygen adsorbed on grain boundaries induces a potential barrier at the grain boundaries through formation of mid-gap energy states, which cause Fermi level pinning.<sup>52</sup> This potential barrier could be formed at the entire interface between ITO and single-crystalline channels. This

potential barrier prevents electron transport across the interfaces, resulting in an increase of contact resistance. On the other hand, in polycrystalline channel devices, this potential barrier should partially cross the interface where electron transport is not prevented. The potential barrier model is also consistent with the huge increase in contact resistance (Figure 2c), which is difficult to be quantitatively explained by only the interfacial dopant Sn deactivation. Although a Sn-dopant deactivation induced by Sn–O<sub>i</sub> clustering and formation of interfacial potential barrier are plausible origins of the observed reversible interfacial resistance change, further investigations such as instability of local structure around dopant Sn within In<sub>2</sub>O<sub>3</sub> at the interface are required to reveal why the reversible interfacial resistance change occurs only at the interface between ITO electrodes and single-crystalline oxide channels.

## CONCLUSIONS

In summary, we demonstrate an unusual reversible dopant activation/deactivation phenomenon, which only emerges at an interface between indium tin oxide (ITO) and single-crystalline oxide channel. We found that the interface electrical resistance between ITO electrodes and single-crystalline oxide nanowire channel can be repeatedly switched between a metallic state and a near-insulative state by applying thermal treatments in air or vacuum. Interestingly, this electrical switching phenomenon disappears when the oxide channel changes from the single-crystalline structure to lithography-defined polycrystalline structure. Atmosphere-controlled annealing experiments reveal that atmospheric oxygen induces the repeatable change in the interfacial electrical resistance. Systematic investigations on metal cation species and channel crystallinity demonstrate that the observed electrical switching is related to an interface-specific reversible Sn-dopant activation/deactivation of ITO electrode in contact with a single-crystalline oxide channel.

## METHODS

**Single-Crystalline Oxide Nanowire Growth.** Sb-doped SnO<sub>2</sub> (ATO) and indium tin oxide (ITO) nanowires were grown on the Al<sub>2</sub>O<sub>3</sub> (110) and (100) substrates by pulsed-laser deposition (PLD) through the vapor–liquid–solid (VLS) process, respectively.<sup>25,26</sup> A 0.7 nm Au film was deposited on the Al<sub>2</sub>O<sub>3</sub> substrates using direct current (DC) sputtering, followed by annealing at 750 °C for 10 min to form agglomerated Au nanoparticle catalysts. Then, ATO or ITO nanowires were grown at 750 °C in 10 Pa of an O<sub>2</sub>/Ar gas mixture (O<sub>2</sub>/Ar = 1:1000, purity: 99.9999%) by an ArF excimer laser (λ = 193 nm, Coherent COMPex-Pro) ablation under the following conditions: pulse repetition time of 10 Hz and laser energy of 40 mJ. SnO<sub>2</sub> mixed with Sb<sub>2</sub>O<sub>3</sub> (1 atom %) and In<sub>2</sub>O<sub>3</sub> mixed with SnO<sub>2</sub> (10 wt %) were utilized as the PLD targets for ATO and ITO nanowires, respectively.

**Device Fabrication.** For oxide nanowire devices, the grown nanowires were dispersed in isopropanol by sonication. The nanowires were then dropped onto a 100 nm SiO<sub>2</sub>/n-type Si substrate. Oxide contact electrodes (20 nm, ITO or ATO) with a 100 nm Pt pad layer were patterned by lift-off processes of electron beam (EB) lithography. ITO electrodes were deposited by radio frequency (RF) sputtering (target: 10 wt % SnO<sub>2</sub> in In<sub>2</sub>O<sub>3</sub>) at room temperature. ATO electrodes were deposited by PLD (target: 10 atom % Sb<sub>2</sub>O<sub>3</sub> in SnO<sub>2</sub>, 10 Pa O<sub>2</sub>, 10 Hz, 60 mJ). After the lift-off, devices with ATO electrodes were annealed at 400 °C for 10 min in air to decrease the electrical resistivity of the sputtered ATO films. For ATO nanobeam devices, the ATO nanobeam channel region was fabricated using EB lithography, PLD, and annealing by the same

process as that of the ATO electrodes of the nanowire devices. ITO/Pt electrodes were then fabricated on the ATO nanobeam by the same process as that of the ITO electrodes of the nanowire devices. For single-crystalline ITO nanofilm devices, a 100 nm ITO thin film was grown on a YSZ (111) substrate at 800 °C in 10 Pa O<sub>2</sub>/Ar (100 ppm O<sub>2</sub> in Ar). SiO<sub>2</sub> (100 nm), which prevents direct current flow from the pads to the ITO channel, was then deposited and patterned using RF sputtering with a stencil mask. ITO/Pt electrodes were then fabricated on the ITO thin film channel by the same process as that of the ITO electrodes of the nanowire devices.

**Characterizations.** The two- and four-probe *I*–*V* characteristics were measured using a semiconductor parameter analyzer (Keithley, 4200SCS) with a probe station having a temperature-controlling system. Resistivity (nanowire:  $\rho_{\text{nw}}$ , electrode:  $\rho_{\text{elec}}$ ) and contact resistivity  $\rho_c$  were extracted from the four-probe measurements of the four-terminal devices.  $\rho_{\text{nw}}$  was calculated by assuming a square nanowire cross section:  $\rho_{\text{nw}} = R_4 W_{\text{nw}}^2 / L_{\text{nw}}$ , where  $R_4$ ,  $W_{\text{nw}}$ , and  $L_{\text{nw}}$  are the four-probe resistance, nanowire width, and length between the two voltage electrodes of each four-terminal device, respectively.  $\rho_{\text{elec}}$  was calculated based on the size-defined rectangle channel of oxide thin-film devices.  $\rho_c$  was calculated as an area-normalized contact resistivity:  $\rho_c = L_c (W + 2H)(R_2 - R_4)$ , where  $W$ ,  $H$ ,  $R_2$ , and  $L_c$  are channel width, channel height, two-probe resistance, and length of contact electrodes on the nanowires, respectively. The dimensions of the nanowires, nanobeam, and electrodes were determined using a field emission scanning electron microscope (FESEM, JEOL, JSM-7610F). For the thermal annealing experiments, annealings were performed at 400 °C for 10 min unless otherwise specified. Dry air (N<sub>2</sub>/O<sub>2</sub> = 4:1, purity: >99%) was used for air annealings. Crystallinity of the fabricated oxide thin film was investigated using XRD (PHILIPS, X'Pert MRD 45 kV, 40 mA). The nanowires observed by STEM were embedded in epoxy resin on the substrate and then thinned by Ar ion milling following mechanical polishing. The HAADF and EDS observations were performed with an accelerating voltage of 200 kV and a convergence semiangle of 22 mrad by an aberration-corrected STEM (JEM-ARM200F) equipped with two silicon drift detectors.

## ■ ASSOCIATED CONTENT

### Supporting Information

The Supporting Information is available free of charge at <https://pubs.acs.org/doi/10.1021/acsami.0c16108>.

XRD pattern of ATO thin film treated by air annealing; annealing time dependence of *I*–*V* characteristics; temperature dependence of resistivity of ITO electrode and ATO nanowire; effects of annealing time and temperature on electrical characteristics; dependence of nanowire resistivity on oxygen pressure during annealing; electrode resistivity, nanowire resistivity, and contact resistivity of oxide nanowire devices; and temperature dependence of contact resistivity (PDF)

## ■ AUTHOR INFORMATION

### Corresponding Authors

**Tsunaki Takahashi** – Department of Applied Chemistry, Graduate School of Engineering, The University of Tokyo, Tokyo 113-8656, Japan; JST, PRESTO, Saitama 332-0012, Japan; [orcid.org/0000-0002-2840-8038](https://orcid.org/0000-0002-2840-8038); Email: [takahashi-t@g.ecc.u-tokyo.ac.jp](mailto:takahashi-t@g.ecc.u-tokyo.ac.jp)

**Takeshi Yanagida** – Department of Applied Chemistry, Graduate School of Engineering, The University of Tokyo, Tokyo 113-8656, Japan; Institute for Materials Chemistry and Engineering, Kyushu University, Fukuoka 816-8580, Japan; [orcid.org/0000-0003-4837-5701](https://orcid.org/0000-0003-4837-5701); Email: [yanagida@g.ecc.u-tokyo.ac.jp](mailto:yanagida@g.ecc.u-tokyo.ac.jp)

## Authors

**Hao Zeng** – Department of Applied Chemistry, Graduate School of Engineering, The University of Tokyo, Tokyo 113-8656, Japan

**Takehito Seki** – Institute of Engineering Innovation, The University of Tokyo, Tokyo 113-8656, Japan

**Masaki Kanai** – Institute for Materials Chemistry and Engineering, Kyushu University, Fukuoka 816-8580, Japan

**Guozhu Zhang** – Institute for Materials Chemistry and Engineering, Kyushu University, Fukuoka 816-8580, Japan

**Takuro Hosomi** – Department of Applied Chemistry, Graduate School of Engineering, The University of Tokyo, Tokyo 113-8656, Japan; JST, PRESTO, Saitama 332-0012, Japan; [orcid.org/0000-0002-5649-6696](https://orcid.org/0000-0002-5649-6696)

**Kazuki Nagashima** – Department of Applied Chemistry, Graduate School of Engineering, The University of Tokyo, Tokyo 113-8656, Japan; JST, PRESTO, Saitama 332-0012, Japan; [orcid.org/0000-0003-0180-816X](https://orcid.org/0000-0003-0180-816X)

**Naoya Shibata** – Institute of Engineering Innovation, The University of Tokyo, Tokyo 113-8656, Japan; [orcid.org/0000-0003-3548-5952](https://orcid.org/0000-0003-3548-5952)

Complete contact information is available at: <https://pubs.acs.org/10.1021/acsami.0c16108>

## Notes

The authors declare no competing financial interest.

## ■ ACKNOWLEDGMENTS

This work was supported by KAKENHI (Grant Numbers JP17H04927, JP18H01831, JP18H05243, and JP18KK0112). T.T. was supported by JST PREST Grant Number JPMJPR19M6, Japan. T.T., G.Z., K.N., and T.Y. were supported by JST CREST Grant Number JPMJCR19I2, Japan. T.Y. and K.N. were supported by CAS–JSPS Joint Research Projects (Grant Number JPJSBP120187207) and by Mirai R&D of JST. The TEM analysis was supported by Nanotechnology Platform project conducted by the Ministry of Education, Culture, Sports, Science and Technology of Japan (Grant Number JPMXP09A19UT0090). This work was performed under the Cooperative Research Program of “Network Joint Research Center for Materials and Devices” and the MEXT Project of “Integrated Research Consortium on Chemical Sciences”.

## ■ REFERENCES

- (1) Ielmini, D.; Wong, H. S. P. In-Memory Computing with Resistive Switching Devices. *Nat. Electron.* **2018**, *1*, 333–343.
- (2) Stornaiuolo, D.; Cantoni, C.; De Luca, G. M.; Di Capua, R.; Di Gennaro, E.; Ghiringhelli, G.; Jouault, B.; Marrè, D.; Massarotti, D.; Granozio, F. M.; Pallecchi, I.; Piamonteze, C.; Rusponi, S.; Tafuri, F.; Salluzzo, M. Tunable Spin Polarization and Superconductivity in Engineered Oxide Interfaces. *Nat. Mater.* **2016**, *15*, 278–283.
- (3) Matsuno, J.; Ogawa, N.; Yasuda, K.; Kagawa, F.; Koshibae, W.; Nagaosa, N. Interface-Driven Topological Hall Effect. *Sci. Adv.* **2016**, *2*, No. e1600304.
- (4) Guo, S.; Li, Q.; Liu, P.; Chen, M.; Zhou, H. Environmentally Stable Interface of Layered Oxide Cathodes for Sodium-Ion Batteries. *Nat. Commun.* **2017**, *8*, No. 135.
- (5) Kattel, S.; Liu, P.; Chen, J. G. Tuning Selectivity of CO<sub>2</sub> Hydrogenation Reactions at the Metal/Oxide Interface. *J. Am. Chem. Soc.* **2017**, *139*, 9739–9754.
- (6) Lee, H.; Campbell, N.; Lee, J. W.; Asel, T. J.; Paudel, T. R.; Zhou, H.; Lee, J. W.; Noesges, B.; Seo, J.; Park, B.; Brillson, L. J.; Oh, S. H.; Tsymbal, E. Y.; Ryzhowski, M. S.; Eom, C. B. Direct

Observation of a Two-Dimensional Hole Gas at Oxide Interfaces. *Nat. Mater.* **2018**, *17*, 231–236.

(7) Kim, T. H.; Puggioni, D.; Yuan, Y.; Xie, L.; Zhou, H.; Campbell, N.; Ryan, P. J.; Choi, Y.; Kim, J. W.; Patzner, J. R.; Ryu, S.; Podkaminer, J. P.; Irwin, J.; Ma, Y.; Fennie, C. J.; Rzchowski, M. S.; Pan, X. Q.; Gopalan, V.; Rondinelli, J. M.; Eom, C. B. Polar Metals by Geometric Design. *Nature* **2016**, *533*, 68–72.

(8) Zhao, X.; Wang, P.; Gao, Y.; Xu, X.; Yan, Z.; Ren, N. CuO/ZnO Core/Shell Nanowire Arrays and Their Photovoltaics Application. *Mater. Lett.* **2014**, *132*, 409–412.

(9) Zhao, Y.; Wang, C.; Wallace, G. G. Tin Nanoparticles Decorated Copper Oxide Nanowires for Selective Electrochemical Reduction of Aqueous CO<sub>2</sub> to CO. *J. Mater. Chem. A* **2016**, *4*, 10710–10718.

(10) Xia, X.; Tu, J.; Zhang, Y.; Wang, X.; Gu, C.; Zhao, X. B.; Fan, H. J. High-Quality Metal Oxide Core/Shell Nanowire Arrays on Conductive Substrates for Electrochemical Energy Storage. *ACS Nano* **2012**, *6*, 5531–5538.

(11) Nakamura, K.; Takahashi, T.; Hosomi, T.; Seki, T.; Kanai, M.; Zhang, G.; Nagashima, K.; Shibata, N.; Yanagida, T. Redox-Inactive CO<sub>2</sub> Determines Atmospheric Stability of Electrical Properties of ZnO Nanowire Devices through a Room-Temperature Surface Reaction. *ACS Appl. Mater. Interfaces* **2019**, *11*, 40260–40266.

(12) Léonard, F.; Talin, A. A. Electrical Contacts to One- and Two-Dimensional Nanomaterials. *Nat. Nanotechnol.* **2011**, *6*, 773–783.

(13) Briseno, A. L.; Holcombe, T. W.; Boukai, A. I.; Garnett, E. C.; Shelton, S. W.; Frechet, J. J.; Yang, P. Oligo- and Polythiophene/ZnO Hybrid Nanowire Solar Cells. *Nano Lett.* **2010**, *10*, 334–340.

(14) Tomioka, K.; Yoshimura, M.; Fukui, T. A III–V Nanowire Channel on Silicon for High-Performance Vertical Transistors. *Nature* **2012**, *488*, 189–192.

(15) Bierman, M. J.; Jin, S. Potential Applications of Hierarchical Branching Nanowires in Solar Energy Conversion. *Energy Environ. Sci.* **2009**, *2*, 1050–1059.

(16) Yu, X.; Marks, T. J.; Facchetti, A. Metal Oxides for Optoelectronic Applications. *Nat. Mater.* **2016**, *15*, 383–396.

(17) Afre, R. A.; Sharma, N.; Sharon, M.; Sharon, M. Transparent Conducting Oxide Films for Various Applications: A Review. *Rev. Adv. Mater. Sci.* **2018**, *53*, 79–89.

(18) Klein, A.; Körber, C.; Wachau, A.; Säuberlich, F.; Gassenbauer, Y.; Harvey, S. P.; Proffitt, D. E.; Mason, T. O. Transparent Conducting Oxides for Photovoltaics: Manipulation of Fermi Level, Work Function and Energy Band Alignment. *Materials*. **2010**, *3*, 4892–4914.

(19) Zhuo, M.; Chen, Y.; Sun, J.; Zhang, H.; Guo, D.; Zhang, H.; Li, Q.; Wang, T.; Wan, Q. Humidity Sensing Properties of a Single Sb Doped SnO<sub>2</sub> Nanowire Field Effect Transistor. *Sens. Actuators, B* **2013**, *186*, 78–83.

(20) Li, F.; Meng, Y.; Dong, R.; Yip, S.; Lan, C.; Kang, X.; Wang, F.; Chan, K. S.; Ho, J. C. High-Performance Transparent Ultraviolet Photodetectors Based on InGaZnO Superlattice Nanowire Arrays. *ACS Nano* **2019**, *13*, 12042–12051.

(21) Liu, X.; Liu, X.; Wang, J.; Liao, C.; Xiao, X.; Guo, S.; Jiang, C.; Fan, Z.; Wang, T.; Chen, X.; Lu, W.; Hu, W.; Liao, L. Transparent, High-Performance Thin-Film Transistors with an InGaZnO/Aligned-SnO<sub>2</sub>-Nanowire Composite and Their Application in Photodetectors. *Adv. Mater.* **2014**, *26*, 7399–7404.

(22) Kim, D. W.; Min, S. Y.; Lee, Y.; Jeong, U. Transparent Flexible Nanoline Field-Effect Transistor Array with High Integration in a Large Area. *ACS Nano* **2020**, *14*, 907–918.

(23) Morales-Masis, M.; De Wolf, S.; Woods-Robinson, R.; Ager, J. W.; Ballif, C. Transparent Electrodes for Efficient Optoelectronics. *Adv. Electron. Mater.* **2017**, *3*, No. 1600529.

(24) Dixon, S. C.; Scanlon, D. O.; Carmalt, C. J.; Parkin, I. P. N-Type Doped Transparent Conducting Binary Oxides: An Overview. *J. Mater. Chem. C* **2016**, *4*, 6946–6961.

(25) Anzai, H.; Suzuki, M.; Nagashima, K.; Kanai, M.; Zhu, Z.; He, Y.; Boudot, M.; Zhang, G.; Takahashi, T.; Kanemoto, K.; Seki, T.; Shibata, N.; Yanagida, T. True Vapor-Liquid-Solid Process Suppresses

Unintentional Carrier Doping of Single Crystalline Metal Oxide Nanowires. *Nano Lett.* **2017**, *17*, 4698–4705.

(26) Zhu, Z.; Suzuki, M.; Nagashima, K.; Yoshida, H.; Kanai, M.; Meng, G.; Anzai, H.; Zhuge, F.; He, Y.; Boudot, M.; Takeda, S.; Yanagida, T. Rational Concept for Reducing Growth Temperature in Vapor-Liquid-Solid Process of Metal Oxide Nanowires. *Nano Lett.* **2016**, *16*, 7495–7502.

(27) Montero, J.; Herrero, J.; Guillén, C. Preparation of Reactively Sputtered Sb-Doped SnO<sub>2</sub> Thin Films: Structural, Electrical and Optical Properties. *Sol. Energy Mater. Sol. Cells* **2010**, *94*, 612–616.

(28) Montero, J.; Guillén, C.; Herrero, J. Discharge Power Dependence of Structural, Optical and Electrical Properties of DC Sputtered Antimony Doped Tin Oxide (ATO) Films. *Sol. Energy Mater. Sol. Cells* **2011**, *95*, 2113–2119.

(29) Montero, J.; Guillén, C.; Herrero, J. Nanocrystalline Antimony Doped Tin Oxide (ATO) Thin Films: A Thermal Restructuring Study. *Surf. Coat. Technol.* **2012**, *211*, 37–40.

(30) Khan, A. F.; Mehmood, M.; Rana, A. M.; Bhatti, M. T. Effect of Annealing on Electrical Resistivity of RF-Magnetron Sputtered Nanostructured SnO<sub>2</sub> Thin Films. *Appl. Surf. Sci.* **2009**, *255*, 8562–8565.

(31) Alsultany, F. H.; Ahmed, N. M.; Matjafri, M. Z. Effects of CW CO<sub>2</sub> Laser Annealing on Indium Tin Oxide Thin Films Characteristics. *Soft Nanosci. Lett.* **2014**, *04*, 83–89.

(32) Wan, Q.; Dattoli, E. N.; Lu, W. Transparent Metallic Sb-Doped SnO<sub>2</sub> Nanowires. *Appl. Phys. Lett.* **2007**, *90*, No. 222107.

(33) Hsu, C. L.; Tsai, T. Y. Fabrication of Fully Transparent Indium-Doped ZnO Nanowire Field-Effect Transistors on ITO/Glass Substrates. *J. Electrochem. Soc.* **2011**, *158*, K20–K23.

(34) Ju, S.; Facchetti, A.; Xuan, Y.; Liu, J.; Ishikawa, F.; Ye, P.; Zhou, C.; Marks, T. J.; Janes, D. B. Fabrication of Fully Transparent Nanowire Transistors for Transparent and Flexible Electronics. *Nat. Nanotechnol.* **2007**, *2*, 378–384.

(35) Shen, G.; Xu, J.; Wang, X.; Huang, H.; Chen, D. Growth of Directly Transferable In<sub>2</sub>O<sub>3</sub> Nanowire Mats for Transparent Thin-Film Transistor Applications. *Adv. Mater.* **2011**, *23*, 771–775.

(36) Huang, J. L.; Pan, Y.; Chang, J. Y.; Yau, B. S. Annealing Effects on Properties of Antimony Tin Oxide Thin Films Deposited by RF Reactive Magnetron Sputtering. *Surf. Coat. Technol.* **2004**, *184*, 188–193.

(37) Ponja, S. D.; Williamson, B. A. D.; Sathasivam, S.; Scanlon, D. O.; Parkin, I. P.; Carmalt, C. J. Enhanced Electrical Properties of Antimony Doped Tin Oxide Thin Films Deposited: Via Aerosol Assisted Chemical Vapour Deposition. *J. Mater. Chem. C* **2018**, *6*, 7257–7266.

(38) Zeng, H.; Takahashi, T.; Kanai, M.; Zhang, G.; He, Y.; Nagashima, K.; Yanagida, T. Long-Term Stability of Oxide Nanowire Sensors via Heavily Doped Oxide Contact. *ACS Sens.* **2017**, *2*, 1854–1859.

(39) Meng, G.; Yanagida, T.; Yoshida, H.; Nagashima, K.; Kanai, M.; Zhuge, F.; He, Y.; Klamchuen, A.; Rahong, S.; Fang, X.; Takeda, S.; Kawai, T. A Flux Induced Crystal Phase Transition in the Vapor-Liquid-Solid Growth of Indium-Tin Oxide Nanowires. *Nanoscale* **2014**, *6*, 7033–7038.

(40) Mason, T. O.; González, G. B.; Hwang, J. H.; Kammler, D. R. Point Defects and Related Properties of Highly Co-Doped Bixbyite In<sub>2</sub>O<sub>3</sub>. *Phys. Chem. Chem. Phys.* **2003**, *5*, 2183–2189.

(41) Warschkow, O.; Ellis, D. E.; Gonzalez, G. B.; Mason, T. O. Defect Structures of Tin-Doped Indium Oxide. *J. Am. Ceram. Soc.* **2003**, *86*, 1700–1706.

(42) Weijtens, C. H. L. Influence of the Deposition and Anneal Temperature on the Electrical-Properties of Indium Tin Oxide. *J. Electrochem. Soc.* **1991**, *138*, 3432–3434.

(43) Yamada, N.; Yasui, I.; Shigesato, Y.; Li, H.; Ujihira, Y.; Nomura, K. Doping Mechanisms of Sn in In<sub>2</sub>O<sub>3</sub> Powder Studied Using <sup>119</sup>Sn Mössbauer Spectroscopy and X-Ray Diffraction. *Jpn. J. Appl. Phys.* **1999**, *38*, No. 2856.

- (44) Nadaud, N.; Lequeux, N.; Nanot, M.; Jove, J.; Roisnel, T. Structural Studies of Tin-Doped Indium Oxide (ITO) and  $\text{In}_4\text{Sn}_3\text{O}_{12}$ . *J. Solid State Chem.* **1998**, *135*, 140–148.
- (45) Warschkow, O.; Ellis, D. E.; Gonzalez, G. B.; Mason, T. O. Defect Cluster Aggregation and Nonreducibility in Tin-Doped Indium Oxide. *J. Am. Ceram. Soc.* **2003**, *86*, 1707–1711.
- (46) Parent, P.; et al. Structural Study of Tin-Doped Indium Oxide Thin Films Using X-Ray Absorption Spectroscopy and X-Ray Diffraction. *J. Electrochem. Soc.* **1992**, *139*, 276.
- (47) Smith, F. T. J.; Lyu, S. L. Effects of Heat-Treatment on Indium-Tin Oxide Films. *J. Electrochem. Soc.* **1981**, *128*, 2388.
- (48) Frank, G.; Kostlin, H. Electrical-Properties and Defect Model of Tin-Doped Indium Oxide Layers. *Appl. Phys. A* **1982**, *27*, 197–206.
- (49) Oba, F.; Kumagai, Y. Design and Exploration of Semiconductors from First Principles: A Review of Recent Advances. *Appl. Phys. Express* **2018**, *11*, No. 060101.
- (50) Ohta, H.; Orita, M.; Hirano, M.; Tanji, H.; Kawazoe, H.; Hosono, H. Highly Electrically Conductive Indium–Tin–Oxide Thin Films Epitaxially Grown on Yttria-Stabilized Zirconia (100) by Pulsed-Laser Deposition. *Appl. Phys. Lett.* **2000**, *76*, 2740–2742.
- (51) Ohta, H.; Orita, M.; Hirano, M.; Hosono, H. Surface Morphology and Crystal Quality of Low Resistive Indium Tin Oxide Grown on Yttria-Stabilized Zirconia. *J. Appl. Phys.* **2002**, *91*, 3547–3550.
- (52) Stucki, F.; Greuter, F. Key Role of Oxygen at Zinc Oxide Varistor Grain Boundaries. *Appl. Phys. Lett.* **1990**, *57*, 446–448.